



The role of iron-oxide aerosols and sunlight in the atmospheric reduction of Hg(II) species: A DFT + *U* study

Sean A. Tacey^a, Tibor Szilvási^a, Lang Xu^a, James J. Schauer^{a,b}, Manos Mavrikakis^{a,*}

^a Department of Chemical and Biological Engineering, 1415 Engineering Drive, University of Wisconsin–Madison, Madison, WI, 53706, USA

^b Department of Civil and Environmental Engineering, 1415 Engineering Drive, University of Wisconsin–Madison, Madison, WI, 53706, USA

ARTICLE INFO

Keywords:

Density functional theory
Iron oxide
Mercury reduction
Photons
Aerosols

ABSTRACT

Experimental and field measurements have shown that, in the presence of both iron-containing aerosols and sunlight, oxidized mercury species such as HgCl₂ and HgBr₂ undergo reduction to elemental mercury (Hg⁰), which remains in the atmosphere longer than oxidized mercury species due to its higher volatility. We performed density functional theory (DFT, PW91 + *U*) calculations to elucidate the reduction mechanism for atmospheric HgCl₂ and HgBr₂ to Hg⁰ on several iron-oxide aerosol surfaces relevant in the troposphere. On the OH-Fe-R-terminated α-Fe₂O₃(0001) surface, predicted to be most prevalent under ambient conditions, we show that: (1) the first Hg-X bond is broken via either thermal or photolytic activation depending on the ambient temperature; (2) photons with an energy of 2.69 eV (461 nm) are required to break the second Hg-X bond; and (3) a photo-induced surface-to-adsorbate charge-transfer process can promote Hg⁰ desorption with an excitation energy of 2.59 eV (479 nm). All the calculated excitation energies are below the threshold value of 3.9 eV (320 nm) for photons in the troposphere, suggesting that sunlight can facilitate mercury reduction on iron-oxide aerosol surfaces. In contrast, the gas-phase reduction of HgCl₂ (HgBr₂) involves photoexcitation requiring an energy of 4.98 (4.45) eV (249 (279) nm); therefore, the energy range of sunlight is not suitable for gas-phase reduction. Our computational results provide the first evidence on the detailed mechanism for the combined role of aerosols and photons in the reduction of HgCl₂ and HgBr₂. Our methodology can be adapted to study other photochemical heterogeneous processes in the atmosphere.

1. Introduction

The mechanism for mercury deposition from the atmosphere to the Earth's surface depends on the chemical form of mercury [1–4]. There are three primary forms of mercury in the atmosphere: elemental gaseous (Hg⁰), oxidized gaseous (Hg(II)), and particulate-bound (Hg(p)) mercury [5,6]. Hg⁰ remains in the atmosphere for months and undergoes global transport due to its high volatility, whereas Hg(II) and Hg(p) species travel locally within ~100 km of the emission source before deposition via either dry or wet deposition processes [7]. Therefore, the physical and chemical transformations among these three forms of mercury have important implications on the length and time scales for atmospheric mercury transport before eventual deposition. In particular, the atmospheric reduction of Hg(II) species to Hg⁰ presents concerns for the widespread accumulation of mercury in the environment, especially in pristine environments that would otherwise have little to no mercury present [5,6,8]. For example, Landis et al. observed upwards of 55% reduction of Hg(II) species to Hg⁰ in coal-fired power plant (CFPP) emission plumes [9]. Furthermore, field studies by de Foy

and coworkers showed that a photochemical reduction reaction step was required to parameterize a chemical box model in order to match the observed reactive mercury concentrations [4]. The main route of exposure from mercury pollution in the environment is through consumption, as inhalation is not of much concern regardless of the chemical form of mercury [10]. One of the primary means by which mercury bioaccumulates through the aquatic food chain is atmospheric deposition. Because Hg⁰ deposits much slower than Hg(II), the reduction reaction leads to widespread accumulation of mercury in otherwise pristine environments [11]. However, there is little fundamental understanding regarding the mechanism for the role of sunlight and aerosols in the Hg(II) reduction process.

Iron-containing aerosols have been shown to promote the reduction of Hg(II) in the presence of photons. Tong et al. showed that the reduction of HgCl₂ to Hg⁰ in a flow-through reactor occurs only in the presence of both a range of aerosols compositions (including FeCl₂ and FeCl₃ aerosols) and a light source [5,6]. In addition, analysis of various CFPP emissions plumes, a primary anthropogenic source of mercury, have shown notable iron concentrations [6,9,12–14]. Natural

* Corresponding author.

E-mail address: manos@engr.wisc.edu (M. Mavrikakis).

atmospheric events also result in the release of iron-containing aerosols to the atmosphere. For example, dust events introduce high regional concentrations of dust aerosols, which contain large numbers of iron-oxide compounds [12–15]. Furthermore, metallic iron released from either an anthropogenic source (e.g., emissions from brake wear [16,17]) or a natural source will ultimately be oxidized to form iron-oxide aerosols. Therefore, iron-oxide aerosols are highly prevalent in the atmosphere and may significantly alter the atmospheric transport and deposition mechanisms for mercury.

Computational chemistry methods present a promising opportunity to study a range of relevant atmospheric aerosols (e.g., iron oxides), as well as to better understand the combined role of photons and aerosols in the Hg(II) reduction chemistry. Previously, we performed density functional theory (DFT) calculations to explore the reduction pathways of various Hg(II) species (e.g., HgCl_2 and HgBr_2) on clean extended surfaces of iron and sodium chloride aerosols [18]. The results of that work showed evidence that the clean iron surface and several high-energy facets of sodium chloride may promote the formation of Hg^0 , but photons may be required for certain steps in the reduction pathway. However, the exact role of photons remains unclear. By studying iron-oxide aerosols, we can directly address the need for photons in the reduction mechanism that has been observed experimentally. Insights gained from this study may also facilitate the development of increasingly more accurate models for atmospheric mercury transport.

This work seeks to explore the reduction mechanism of Hg(II) species on iron-oxide aerosol surfaces and to determine the role of photons in the reduction process. Our work is focused on the reduction of HgCl_2 and HgBr_2 , as Cl and Br species in the atmosphere are common oxidants of elemental mercury both before and after the release of mercury to the atmosphere [19–27]. First, we address why it is not sufficient for photons alone to promote the gas-phase reduction of HgCl_2 and HgBr_2 . We then explore the Hg(II) reduction pathways on atmospherically relevant surface terminations of $\alpha\text{-Fe}_2\text{O}_3(0001)$, the thermodynamically most stable facet of iron oxide, using DFT calculations. Based on the computational results, we postulate what role atmospherically relevant iron-oxide aerosol surfaces serve in the Hg(II) reduction process. By developing an improved understanding for the photolytic reduction of these two Hg(II) species on relevant terminations of the $\alpha\text{-Fe}_2\text{O}_3(0001)$ surface, we can gain mechanistic insights into this chemistry that are lacking in the experimental literature. Importantly, the methodology described here can be adapted to model photochemical processes in the atmosphere involving a range of aerosol surfaces.

2. Methods

All DFT calculations were performed through the Vienna *Ab initio* Simulation Package (VASP) [28,29]. We implemented our calculations via the generalized-gradient approximation (GGA) through the Perdew-Wang 91 (PW91) exchange-correlation functional [30]. To describe electron-ion interactions, we used projector augmented-wave (PAW) potentials with valence electron wave functions expanded using a plane-wave basis set with a cutoff energy of 400 eV [31,32]. To represent the on-site Coulombic repulsions for the $\alpha\text{-Fe}_2\text{O}_3(0001)$ surface, it is standard to add $+U$ corrections to the PW91 energy functional [33–35]. For our study, we used the well-established values of 4.0 and 1.0 eV for the U and J parameters for the iron atoms, respectively [36,37]. In addition, spin-polarized adjustments to the GGA were made to describe the proper magnetic ordering. In accordance with our DFT $+U$ results in this study (see Figure S1 and Table S1), our previous work [38], and findings in the literature [36], we applied a $(+ - +)$ anti-ferromagnetic ordering.

In order to determine which surface terminations of $\alpha\text{-Fe}_2\text{O}_3(0001)$ are most relevant under typical tropospheric conditions, we constructed phase diagrams by considering thirteen surfaces with a range of oxygen, hydroxyl, and water coverage (Figure S3) to simulate the effects of

oxygen partial pressure (p_{O_2}) and relative humidity ($x_{\text{H}_2\text{O}}$) in the atmosphere. Our approach follows a similar methodology as in our previous work on iron-oxide surfaces [38]. While $+U$ corrections are the current standard for electronic-structure calculations involving iron-oxide surfaces, previous findings suggest that GGA calculations provide better agreement with experimental results regarding the preferentially exposed surface terminations than those using GGA $+U$ [39]. Therefore, we constructed phase diagrams using both PW91 and PW91 $+U$. To produce these phase diagrams, we calculated the surface free energy (γ) for each surface termination as a function of p_{O_2} and $x_{\text{H}_2\text{O}}$ by Eq. (1):

$$\gamma = \frac{1}{A} \left[E_{\text{slab}} - \frac{1}{2} N_{\text{Fe}} \epsilon_{\text{Fe}_2\text{O}_3}^{\text{bulk}} + \frac{1}{4} (3N_{\text{Fe}} - 2N_{\text{O}} + N_{\text{H}}) \mu_{\text{O}_2} - \frac{1}{2} N_{\text{H}} \mu_{\text{H}_2\text{O}} \right] \quad (1)$$

In Eq. (1), A is the area of the slab surface, E_{slab} is the total energy of the clean slab, $\epsilon_{\text{Fe}_2\text{O}_3}^{\text{bulk}}$ is the total energy of one formula unit (one Fe_2O_3 group) of bulk $\alpha\text{-Fe}_2\text{O}_3$, N_i is the number of i atoms in the slab unit cell, and μ_k is the chemical potential of species k . Detailed derivations for these equations, as well as equations for the chemical potential of O_2 and H_2O (which are functions of p_{O_2} and $x_{\text{H}_2\text{O}}$, respectively) are provided in the Supporting Information.

We modeled each surface using a (2×2) surface unit cell repeated in a supercell geometry. Depending on the termination, each slab had 8 or 9 layers, with the bottom four layers fixed in their truncated bulk positions and the remaining layers allowed to fully relax. We separated any pair of successive slabs along the z -axis using a vacuum layer thickness of 16 Å. For bulk $\alpha\text{-Fe}_2\text{O}_3(0001)$, our calculated lattice parameters are 5.068 Å and 2.738 for PW91 $+U$ and 4.998 and 2.769 for PW91 for a and c/a , respectively, both in good agreement with experimental values of 5.035 Å and 2.730 [40]. The surface Brillouin zone was sampled via a $2 \times 2 \times 1$ Monkhorst-Pack k -point mesh [41]. Adsorption of the relevant intermediates in the reduction pathway for Hg(II) to Hg^0 was limited to one exposed facet of the slab, with necessary adjustments made to the electrostatic potential [42,43]. Each structure was relaxed until the Hellmann-Feynman forces acting upon each atom were less than or equal to 0.02 eV/Å. Convergence of reported values was ensured with respect to all calculation parameters to 0.01 eV.

Binding energies (E_{B}) were calculated for the relevant surface intermediates in the reduction pathway of HgCl_2 (HgBr_2) to Hg^0 and Cl_2 (Br_2). Binding energies were determined relative to the energies of both the clean slab (E_{slab}) and the adsorbate in the gas phase (E_{gas}), giving Eq. (2):

$$E_{\text{B}} = E_{\text{total}} - E_{\text{slab}} - E_{\text{gas}}, \quad (2)$$

where E_{total} is the total energy of the system with the adsorbate present on the surface. To obtain the activation energy barriers (E_{a}) for the elementary steps in the Hg(II) reduction pathway, we performed climbing-image nudged elastic band (CI-NEB) calculations [44,45]. We interpolated seven images between the initial and final states in the CI-NEB calculations. For all images, the residual forces were converged to below 0.1 eV/Å. The transition states were verified by the presence of a single imaginary mode in the vibrational analyses [46]. By combining thermochemical (E_{B}) and kinetic (E_{a}) parameters, we constructed the energy profiles mapping the energetics for HgCl_2 and HgBr_2 reduction on each of the studied iron-oxide surfaces.

The role of photons in the reduction of HgCl_2 and HgBr_2 on the selected iron-oxide surfaces was probed via a combination of Bader charge and direct band-excitation calculations. The Bader charge analysis was implemented to determine the charge state of each individual atom in our system using the method provided by Henkelman et al. [47–50]. To estimate excitation energies for Hg-containing species on the iron-oxide surfaces, we plotted the total density of states and partial density of states of mercury. Using this information, we obtained the band corresponding to the lowest-unoccupied orbital for the mercury atom. Our excitation energy calculation was then performed by moving an electron to this band from the valence band maximum of the iron-

Table 1

Excitation energies (E_{Excite}), corresponding photon wavelengths (ν_{Excite}), and bond lengths ($d_{\text{Hg-X}}$) for gas-phase HgCl, HgBr, HgCl₂, and HgBr₂ in the S_0 and S_1 states.

Species	This work				Literature [63]
	E_{Excite} (eV)	ν_{Excite} (nm)	$d_{\text{Hg-X}}(S_0)$ (Å)	$d_{\text{Hg-X}}(S_1)$ (Å)	
HgCl	2.07	599	2.42	3.18	–
HgBr	1.76	704	2.55	3.39	–
HgCl ₂	4.98	249	2.27	2.65	5.18
HgBr ₂	4.45	279	2.40	3.22	–

oxide surface and taking the energy difference between this excited state and the ground state. This method is known in the literature as the ΔSCF method. Although this is a very simple approximation, it still yields relatively accurate excitation energies (within 0.3–0.5 eV) [51,52].

Gas-phase excitation energies were calculated by time-dependent density functional theory (TD-DFT) calculations as implemented in *Gaussian09* [53]. We used the PBE0 hybrid functional [54,55] with basis sets including diffuse functions (Hg: aug-cc-pVDZ-PP [56,57]; Cl and Br: Def2-SVPD [58–61]). We evaluated the specific theoretical method and found that it provided agreement within 0.2 eV with known experimental literature values (see details in the Results and Discussion section and Table 1).

3. Results and discussion

3.1. Homogeneous gas-phase reduction of Hg(I) and Hg(II) species

Before addressing the combined role of photons and iron-oxide aerosols in the reduction of HgCl₂ and HgBr₂, we first probed the energetics for the photolytic gas-phase reduction mechanism. Data from the NIST-JANAF thermochemical tables indicate that at 298 K, the homolytic dissociation of HgCl₂(g) HgBr₂(g) to Hg⁰ and 2 Cl(g) (2Br(g)) is endothermic by 4.67 eV (3.84 eV) [62]. The large endothermicity indicates that thermal effects alone cannot promote this reduction process; i.e., photons are needed. Therefore, we calculated the excitation energies for HgCl, HgBr, HgCl₂, and HgBr₂ from the ground state (S_0) to the first singlet excited state (S_1). The excitation energies are summarized in Table 1. Based on these calculations, the energy required to excite an electron from the S_0 ground state to the S_1 state is notably larger for the Hg(II) species than that for the respective Hg(I) species (by 2.91 and 2.69 eV for the HgCl_x and HgBr_x species, respectively). We also find that the excitation energies required to promote Hg-X bond dissociation are lower for the HgBr_x species as compared to the HgCl_x species. This finding is likely due to the aforementioned lower bond energies noted from the NIST-JANAF thermochemical tables.

Electronic excitation does not necessarily result in bond dissociation. To determine the propensity for bond dissociation in HgCl, HgBr, HgCl₂, and HgBr₂, we examined the change in Hg-X bond length upon excitation (Table 1), as well as the highest-occupied (HOMO) and lowest-unoccupied molecular orbitals (LUMO) (Figure S2). For each species, the HOMO involves a lone pair on the halogen atom(s), whereas the LUMO is the Hg-X anti-bonding orbital primarily involving the 6s orbital of mercury. Excitation to anti-bonding orbitals is essential for bond dissociation [64]. For gas-phase HgCl₂ (HgBr₂) species, excitation of an electron from the HOMO to the LUMO results in the reduction of Hg(II) to Hg(I) by oxidizing the Cl[−] (Br[−]) anion to atomic Cl (Br). In addition, notable bond stretching occurs upon excitation to the S_1 state, ranging from 16.7% to 34.2% stretching for HgCl₂ and HgBr₂, respectively. As a result, our calculations provide strong indications that if an electron is excited from the HOMO to the LUMO in any of the gas-phase Hg(II) or Hg(I) species studied, bond dissociation

can occur.

These results are consistent with experimental findings available in the literature. It has been postulated that Hg(I) species are unstable and readily decompose to Hg⁰ in the atmosphere as compared to the respective more stable Hg(II) species [5,7,65]. The instability of the Hg(I) species is likely due to the low calculated excitation energies: 2.07 and 1.76 eV for gas-phase HgCl and HgBr, respectively. These excitation energies correspond to photons in the visible light and infrared regions of the spectrum, respectively, which are abundant in the troposphere. Conversely, the reduction of HgCl₂ and HgBr₂ to Hg⁰ likely requires photons and other components as well (such as aerosols) due to the high excitation energies (4.98 and 4.45 eV, respectively). Because the stratosphere filters out high-energy photons with wavelengths less than 320 nm (3.9 eV) [66], the excitation energies for these two Hg(II) species cannot be overcome by photons alone in the troposphere. Thus, a key role for aerosols in atmospheric Hg(II) reduction chemistry may be to lower the excitation energy, as bond dissociation becomes favorable once electron excitation occurs.

3.2. Tropospherically relevant iron-oxide surface terminations

Here, we developed phase diagrams to probe which iron-oxide surfaces are most relevant under tropospherically relevant conditions. In these phase diagrams, we tested 13 different surface terminations (Figure S3) that cover a range of surface coverage of O and OH and a test case for low H₂O coverage to see if water coverage may be important. As discussed in the Methods section, we developed phase diagrams using both PW91 and PW91 + U levels of theory. The results of our phase diagram analysis are provided in Fig. 1.

Under a fixed oxygen partial pressure of 0.21 bar, a temperature range of −20–40 °C, and a relative humidity range of 0.01–1, the oxygen and water chemical potentials fall within roughly 0.1–0.2 eV of −10.3 eV and −14.3 eV, respectively. The white lines in each phase diagram depict the relevant range of chemical potentials for each species under typical tropospheric conditions. The intersection of the two ranges (Region A in both phase diagrams) indicates the typical ambient conditions; accordingly, both phase diagrams predict the OH-Fe-R-terminated surface to be most stable under the typical conditions in the troposphere, where R denotes the bulk $\alpha\text{-Fe}_2\text{O}_3(0001)$ ordering. If we take into consideration the maximum DFT error of 0.2 eV [67] (yellow box surrounding Region A in Fig. 1), the (OH)₃-Fe-R and (OH)₃-R surface terminations may also be stable based on the PW91 and PW91 + U phase diagrams, respectively. Additionally, under dry conditions ($x_{\text{H}_2\text{O}} \sim 0$), our PW91 phase diagram (Region B) predicts the O-Fe-R surface termination to be most stable. Lastly, when the relative humidity approaches zero, the Fe-O₃-R (Region C) or O₃-R (Region D) surface terminations will be stable under oxygen-poor or oxygen-rich conditions, respectively. Because the literature shows that + U corrections do not accurately describe the role of oxygen chemical potential on the $\alpha\text{-Fe}_2\text{O}_3(0001)$ surface termination [39], we only performed our dry-condition analysis on the PW91 phase diagram.

While both phase diagrams predict the OH-Fe-R termination to be most stable, we also consider the Fe-O₃-R, O-Fe-R, O₃-R, (OH)₃-Fe-R, and (OH)₃-R surface terminations (the six surfaces are depicted in Fig. 2). The results of our phase diagram analysis are consistent with those in our previous work on iron-oxide surfaces using a different level of theory (PBE with dDsC dispersion corrections included) [38].

3.3. Energy profile for Hg(II) reduction on $\alpha\text{-Fe}_2\text{O}_3(0001)$ surfaces

After confirming that either thermal effects or photons alone are not sufficient to promote the gas-phase reduction for the studied Hg(II) species, we then mapped the reduction pathway for HgCl₂ (HgBr₂) to Hg and Cl₂ (Br₂) on the six iron-oxide surface terminations identified through our phase diagram analysis (Fig. 3 and S4, respectively). To construct these reaction energy profiles, we calculated the binding

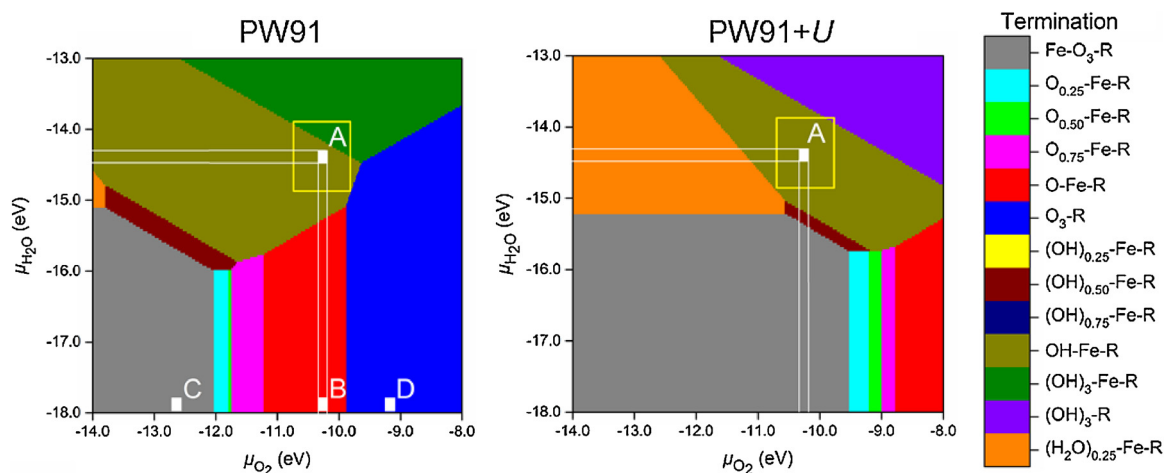


Fig. 1. PW91 (left) and PW91 + *U* (right) phase diagrams for the α -Fe₂O₃(0001) surface as a function of oxygen and water chemical potential. The vertical white dashed lines represent the following range of gas-phase conditions: $p_{\text{O}_2} = 0.21$ bar, $T = -20$ – 40 °C, and $x_{\text{H}_2\text{O}} = 0.01$ – 1 . Regions A–D denote the tropospherically relevant regions discussed in the main text. The yellow box surrounding region A represents the range of DFT error (± 0.2 eV) (For interpretation of the references to color in this figure legend, the reader is referred to the web version of this article).

energy for each surface intermediate (Table S2) as well as the reaction energy and activation energy barrier for each elementary step in the reduction pathway (Tables S3 and S4). This section is presented as follows: First, the strengths of adsorption of HgCl₂ and HgBr₂ on each of the studied iron-oxide surfaces are discussed; second, an analysis of the activation of the two Hg–X bonds ($X = \text{Cl}$ or Br) is provided; third, information regarding the desorption of atomic mercury from each of the studied surfaces is detailed; and fourth, an overview regarding the energetics required to remove atomic Cl (Br) as Cl₂ (Br₂) from each surface is presented. Unless otherwise noted, in each of the following subsections, we provide the results for each of the six surfaces in small paragraphs in the following order: (1) OH–Fe–R; (2) (OH)₃–Fe–R and (OH)₃–R; (3) O–Fe–R; and (4) Fe–O₃–R and O₃–R.

Based on the rule of thumb that the rate of a reaction doubles with a 10 K increase in temperature [68], we estimate that there is roughly 0.4–0.6 eV of energy available to the system under the temperature range of -20 to 40 °C typical of the troposphere. Therefore, when determining whether thermal effects can promote a step in the energy profiles for HgCl₂ and HgBr₂ reduction, we employ a cutoff range of 0.4–0.6 eV.

3.3.1. Adsorption of HgCl₂ and HgBr₂

First, we studied the adsorption of HgCl₂ and HgBr₂ on the six terminations of the α -Fe₂O₃(0001) surface, with the results for each surface summarized in Figs. 3 and S4 for HgCl₂ and HgBr₂, respectively. HgCl₂ (HgBr₂) adsorbs on the OH–Fe–R-terminated surface with a binding energy of -0.53 (-0.52) eV. Our findings show that both species have similar adsorption energies. Further, the adsorption energies for HgCl₂ and HgBr₂ on the OH–Fe–R surface suggest that both species might desorb at higher tropospheric temperatures.

On the (OH)₃–Fe–R- and (OH)₃–R-terminated α -Fe₂O₃(0001) surfaces, HgCl₂ (HgBr₂) adsorbs with binding energies of -0.30 (-0.26) and -0.45 (-0.38) eV, respectively. As a result, desorption of these molecules from these surfaces is even more competitive than that from the OH–Fe–R termination.

On the O–Fe–R α -Fe₂O₃(0001) surface termination, HgCl₂ (HgBr₂) adsorbs to the surface with a binding energy of -0.25 (-0.46) eV. Similar to the three hydroxylated surface terminations, we expect the desorption of HgCl₂ and HgBr₂ from this surface to compete with the subsequent surface reaction steps.

On the Fe–O₃–R surface, the adsorption energy is -1.64 (-1.53) eV. On the O₃–R surface, spontaneous Hg–X bond dissociation occurs upon adsorption, leaving HgCl (HgBr) and Cl (Br) adsorbed on the surface

with a dissociative adsorption energy of -1.77 (-1.91) eV, where the dissociative adsorption energy is the reaction energy for $\text{HgX}_2(\text{g}) \rightarrow \text{HgX}^* + \text{X}^*$ (where $*$ denotes an adsorbed species). On these two surface terminations, desorption is minimal due to large adsorption energies for HgCl₂ (HgBr₂).

3.3.2. Hg–X bond dissociation

Once HgCl₂ and HgBr₂ are adsorbed on the surface, the Hg–X bonds must be broken to form elemental mercury on the surface. In our analysis, we obtained all results at infinite separation. For example, for the adsorbed HgCl bond-dissociation step, we do not consider the presence of the Cl surface intermediate from the initial bond dissociation in HgCl₂. This is because iron-oxide aerosols in the atmosphere are several orders-of-magnitude ($O(10^3)$) more abundant than gas-phase HgCl₂ or HgBr₂ [6], indicating that clean aerosol surfaces may be readily available in the atmosphere for the mercury reduction reaction. As a result, we expect that surface chemistry is taking place at the low-coverage limit.

On the OH–Fe–R-terminated surface, the complete bond dissociation (i.e., to break both Hg–X bonds) is exothermic by -0.58 (-1.50) eV, with activation energy barriers of 0.51 (0.31) and 0.92 (0.60) eV to dissociate the first and second bond in HgCl₂ (HgBr₂), respectively (Fig. 3 (S4), dark yellow line). The barriers for breaking the first bond in HgCl₂ and both bonds in HgBr₂ are relatively small, and thermal energy might be sufficient to overcome them, although photons may help in the first dissociation step in HgCl₂ and the second dissociation step HgBr₂. However, the second Hg–Cl bond dissociation has a high barrier (0.92 eV), and electronic excitation via photons can be essential to promote this dissociation at tropospheric conditions. Also, we observe that both activation barriers for adsorbed HgBr₂ are lower than those for adsorbed HgCl₂.

On the (OH)₃–R-terminated surface, the complete decomposition of HgCl₂ (HgBr₂) is highly endothermic by 2.33 (3.18) eV with endothermicities of 1.17 (1.66) and 1.16 (1.52) eV for the first and second bond-dissociation events, respectively (Fig. 3 (S4), purple line). On the (OH)₃–Fe–R-terminated surface, the first bond-breaking step is barrierless for HgCl₂ (HgBr₂) and exothermic by -2.80 (-3.02) eV; the second bond-breaking step is endothermic by 1.37 (1.80) eV. The overall process is exothermic by -1.43 (-1.22) eV (Fig. 3 (S4), green line). For both HgCl₂ and HgBr₂, the first bond-breaking step on the (OH)₃–Fe–R surface is spontaneous in the forward direction, while the second bond-breaking step on the (OH)₃–Fe–R surface and both steps on the (OH)₃–R surface are spontaneous in the reverse direction.

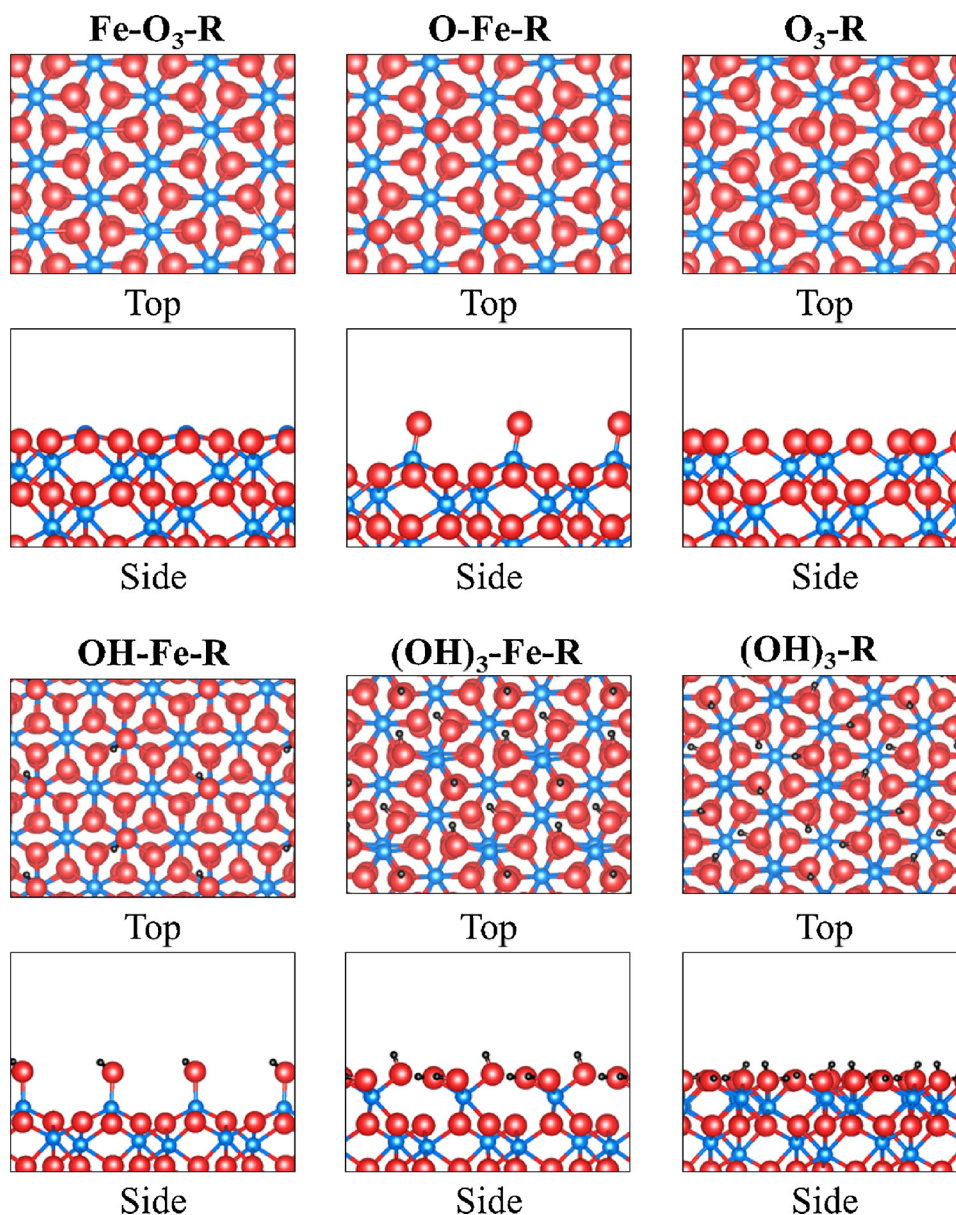


Fig. 2. Top and cross-sectional (side) views of each of the six studied $\alpha\text{-Fe}_2\text{O}_3(0001)$ surface terminations. Atom colors are: blue – Fe, red – O, and black – H (For interpretation of the references to color in this figure legend, the reader is referred to the web version of this article).

On the O-Fe-R surface, the complete decomposition of HgCl_2 (HgBr_2) is highly exothermic by -2.91 (-3.84) eV. For HgCl_2 , activation energy barriers of 0.24 and 0.04 eV need to be overcome to dissociate the first and second Hg-Cl bonds, respectively (Fig. 3, red line). For adsorbed HgBr_2 , both Hg-Br bonds are broken in a single step with an activation energy barrier of 0.05 eV (Figure S4, red line).

On the Fe-O₃-R surface, the complete HgCl_2 (HgBr_2) decomposition is endothermic by 1.00 (1.26) eV. For HgCl_2 , the first bond-breaking step has an activation energy barrier of 0.98 eV, whereas the activation energy barrier for the second step is 0.21 eV (Fig. 3, grey line). Similar to the O-Fe-R surface termination, both Hg-Br bonds in adsorbed HgBr_2 are broken in a single concerted step, which is endothermic by 1.26 eV (Figure S4, grey line). For the O₃-R-terminated surface, as discussed in Section 3.3.1, the first bond-breaking event for both species occurs spontaneously upon adsorption. The subsequent bond-breaking step has an activation energy barrier of 0.58 (0.26) eV with a reaction energy of -0.50 (-0.73) eV (Fig. 3 (S4), blue line).

Based on our results, we expect that complete HgX_2 decomposition readily occurs on the O-Fe-R-terminated $\alpha\text{-Fe}_2\text{O}_3(0001)$ surface for

both species, as well as for HgBr_2 on the O₃-R-terminated surface, under typical ambient conditions. On each of the remaining surfaces, one or both dissociation steps are energetically unfavorable, and to overcome the energy barriers requires more energy than is thermally available at ambient conditions. These findings suggest either that these surfaces are not relevant for the mercury reduction chemistry, or that photons are needed to promote photolytic bond dissociation, which will be discussed in Section 3.4.1. A summary of elementary steps in which photons may be required to promote Hg-X bond breaking on each of the studied surfaces is provided in Table 2.

3.3.3. Desorption of elemental mercury

Once the Hg-X bonds in adsorbed HgCl_2 and HgBr_2 are broken, elemental mercury must desorb from the iron-oxide surface to complete the mercury reduction process. The mercury desorption energy for each surface is provided in the HgCl_2 and HgBr_2 reduction energy profiles in Figs. 3 and S4, respectively. Here, we present the mercury desorption results in two groups: (1) the surfaces with binding energies weaker than -0.3 eV and (2) the surfaces with strong adsorption (i.e., binding

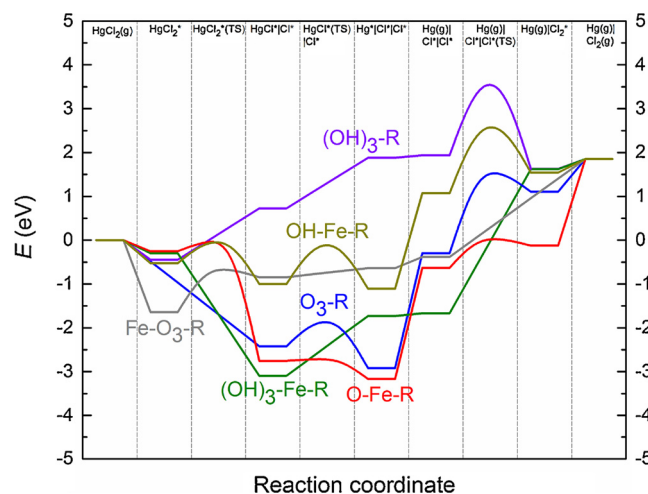


Fig. 3. Energy profile for the reduction of HgCl_2 on the six studied $\alpha\text{-Fe}_2\text{O}_3(0001)$ surface terminations. Note: | signifies infinite separation; * and (g) denote adsorbed and gas-phase species, respectively. Curved lines represent the transition states. We note that there are no transition states for the second Hg-Cl bond-breaking and Cl_2 recombination steps on the $\text{Fe-O}_3\text{-R}$ surface, all elementary steps on the $(\text{OH})_3\text{-Fe-R}$ surface, and all but the Cl_2 recombination step on the $(\text{OH})_3\text{-R}$ surface, because these steps are spontaneous in the exothermic direction. Also, HgCl_2 adsorbs dissociatively as HgCl^* and Cl^* on the $\text{O}_3\text{-R}$ surface, so the HgCl_2^* and $\text{HgCl}_2^*(\text{TS})$ states are not present on this surface.

Table 2

Promotion by photons in the HgCl_2 and HgBr_2 reduction mechanism. “X” indicates that the step may necessitate photons (using the criterion described in the text), whereas “–” denotes that the step does not require photons. The results for the OH-Fe-R -terminated surface are in bold as this is predicted to be the most stable termination of $\alpha\text{-Fe}_2\text{O}_3(0001)$ under typical tropospheric conditions. Note: “*” signifies that both Hg-X bonds are broken in a single concerted step, and “†” specifies that the reaction step may or may not need photons, depending on the ambient temperature.

Species	Surface	1 st Hg-X bond dissociation step	2 nd Hg-X bond dissociation step	Hg desorption step
HgCl_2	$\text{Fe-O}_3\text{-R}$	X	–	–
	O-Fe-R	–	–	X
	$\text{O}_3\text{-R}$	–	X^\dagger	X
	OH-Fe-R	X^\dagger	X	X
	$(\text{OH})_3\text{-Fe-R}$	–	X	–
	$(\text{OH})_3\text{-R}$	X	X	–
HgBr_2	$\text{Fe-O}_3\text{-R}$	X^*	X^*	–
	O-Fe-R	–*	–*	X
	$\text{O}_3\text{-R}$	–	–	X
	OH-Fe-R	–	X^\dagger	X
	$(\text{OH})_3\text{-Fe-R}$	–	X	–
	$(\text{OH})_3\text{-R}$	X	X	–

energies larger than 2 eV in magnitude).

Elemental mercury adsorbs the weakest to the $(\text{OH})_3\text{-R}$ and $(\text{OH})_3\text{-Fe-R}$ surfaces, with adsorption energies of -0.05 and -0.06 eV, respectively. On the $\text{Fe-O}_3\text{-R}$ surface, the adsorption is slightly stronger at -0.25 eV. Therefore, if Hg-X bond dissociation occurs on any of these three surfaces, it is likely that elemental mercury readily desorbs from the surfaces, thereby completing the mercury reduction process.

On the three remaining surfaces the adsorption energies for mercury are significantly stronger: -2.18 , -2.54 , and -2.62 eV on the OH-Fe-R , O-Fe-R , and $\text{O}_3\text{-R}$ iron-oxide surface terminations, respectively. Consequently, if the Hg-Cl and Hg-Br bonds are broken on these surfaces leaving adsorbed mercury, it is very difficult to complete the mercury reduction process through the removal of mercury as Hg^0 from these three surfaces. Observations of the mercury adsorption structures depicted in Table S2 reveal that strong mercury adsorption occurs due

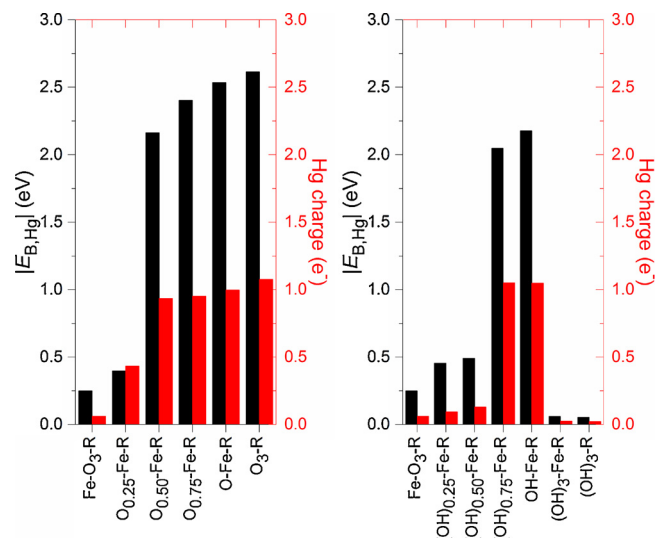


Fig. 4. Adsorption energy (in black) versus Bader charge on Hg (in red) as a function of increasing oxygen (left) and hydroxyl (right) coverage (For interpretation of the references to color in this figure legend, the reader is referred to the web version of this article).

to the stabilizing interactions with unsaturated surface oxygen or hydroxyl species. Conversely, there are no unsaturated O or OH surface species on the $\text{Fe-O}_3\text{-R}$, $(\text{OH})_3\text{-R}$, and $(\text{OH})_3\text{-Fe-R}$ surface terminations, resulting in a decrease in the adsorption energy, as previously discussed.

To show the effect of these unsaturated surface O and OH species on the adsorption strength of mercury, we examined the relationship between the adsorption energy and the Bader charge of the mercury atom adsorbed on the iron-oxide surface (see Fig. 4). Our results show a strong correlation between these two quantities. The calculated Bader charges indicate that mercury adsorbs in an oxidized state on the OH-Fe-R , O-Fe-R , and $\text{O}_3\text{-R}$ $\alpha\text{-Fe}_2\text{O}_3(0001)$ surface terminations. On these three surfaces, there are unsaturated, negatively charged oxygen/hydroxyl species that can interact with the adsorbed mercury. Because mercury adsorbs in a cationic state on these surfaces, Coulombic interactions with the surrounding negatively charged oxygen/hydroxyl species lead to strong adsorption. For example, mercury adsorbs on the OH-Fe-R in an oxidized state with a Bader charge of $+1.05 e^-$, resulting in a large adsorption energy of -2.18 eV. On the other hand, according to the trends shown in Fig. 4, a neutral mercury atom binds very weakly (weaker than -0.3 eV) on iron-oxide surfaces and can easily desorb from the surface. Thus, photons may play a role in mercury desorption by exciting an electron from the iron-oxide surface to the adsorbed mercury, which decreases the adsorption strength of mercury and promotes the formation of gas-phase Hg^0 .

Our results, therefore, indicate another potential role of photons in the reduction mechanism for HgCl_2 and HgBr_2 . For example, on the OH-Fe-R $\alpha\text{-Fe}_2\text{O}_3(0001)$ surface termination, predicted to be the most stable under typical atmospheric conditions, photons may be responsible for assisting in the desorption of mercury as Hg^0 following Hg-Cl and Hg-Br bond-dissociation steps. This potential role will be discussed further in Section 3.4.2. A summary of the surfaces in which photons may be required to promote the desorption of mercury (i.e., the OH-Fe-R , O-Fe-R , and $\text{O}_3\text{-R}$ iron-oxide surfaces) is provided in Table 2.

3.3.4. Desorption of Cl (Br) as Cl_2 (Br_2)

Once mercury desorbs from the surface, mercury reduction is complete. However, following mercury desorption (as in our reaction energy profiles in Figs. 3 and S4), there are still two Cl (Br) atoms adsorbed on the surface as the result of the HgX_2 decomposition reaction. To clean the surface and complete the catalytic cycle, these atomic

halide species need to be desorbed from the surfaces as Cl_2 and Br_2 .

On the OH-Fe-R surface, the formation of the Cl_2 (Br_2) surface intermediate has an activation barrier of 1.56 (0.95) eV. Then, the desorption of the halogen intermediate from the OH-Fe-R surface requires 0.31 (0.50) eV. As a result, the formation of the surface intermediates is not possible under tropospheric conditions, although the formation barrier for Br_2 is lower than that for Cl_2 . However, if the intermediates are formed, Cl_2 readily desorbs from the surface while Br_2 likely only desorbs at higher tropospheric temperatures.

The formation and desorption of Cl_2 (Br_2) from the $(\text{OH})_3\text{-R}$ surface requires energies of 1.68 (0.26) eV and 0.23 (0.33) eV, respectively. Therefore, while the formation of the Cl_2 surface intermediate will not occur in the troposphere, the formation and subsequent desorption of Br_2 from the $(\text{OH})_3\text{-R}$ surface is favorable. On the $(\text{OH})_3\text{-Fe-R}$ -terminated surface, the activation barrier to form the Cl_2 (Br_2) surface intermediate was calculated as 3.29 (2.64) eV. These significant barriers indicate that Cl_2 and Br_2 cannot be formed on the surface; even with the low calculated desorption barrier of 0.23 (0.38) eV for Cl_2 (Br_2), atomic Cl (Br) cannot be removed from the $(\text{OH})_3\text{-Fe-R}$ surface.

The removal of atomic Cl (Br) from the O-Fe-R does not likely occur due to the activation barrier of 0.66 (1.46) eV to form the Cl_2 (Br_2) surface intermediate, as well as the high desorption barrier of 1.97 (2.11) eV. Our reaction energy profiles indicate that on the $\text{Fe-O}_3\text{-R}$ $\alpha\text{-Fe}_2\text{O}_3(0001)$ surface termination, direct desorption of both Cl (Br) atoms as gas-phase Cl_2 (Br_2) can take place but is endothermic by 2.24 (1.63) eV. On the $\text{O}_3\text{-R}$ surface, the formation of the Cl_2 (Br_2) surface intermediate has an activation barrier of 1.86 (1.47) eV, and desorption of this intermediate requires 0.75 (1.21) eV. Thus, it is unlikely that Cl_2 (Br_2) is removed to the gas phase on either of these two surfaces.

Aside from atomic Br on the $(\text{OH})_3\text{-R}$ surface, our results suggest that it is unlikely that atomic Cl and Br are thermally removed from the surface, and a buildup of halide coverage could be created during the reduction reaction. As discussed in section 3.3.2, iron-oxide aerosols are ~1000 times more abundant than gas-phase HgCl_2 or HgBr_2 in the atmosphere [6]. Because clean aerosol surfaces may be readily available in the atmosphere for the mercury reduction reaction, halide desorption is not necessarily relevant to understanding mercury reduction on the considered iron-oxide surfaces, and we do not explicitly address the role of halide coverage in the Hg(II) reduction pathway on iron-oxide aerosols.

3.4. Combined role of photons and iron-oxide aerosols in Hg(II) reduction

By mapping the energy profile for HgCl_2 and HgBr_2 reduction on each of the six studied $\alpha\text{-Fe}_2\text{O}_3(0001)$ surfaces, we identified three potential roles for photons in the reduction pathway: (1) after HgCl_2 and HgBr_2 adsorb to the iron-oxide surface, photons may be necessary to help promote bond activation to create elemental mercury on the surface; (2) photons may assist in atomic mercury desorption through a surface-to-adsorbate charge-transfer mechanism, particularly on surfaces which adsorb mercury strongly (> 0.5 eV in magnitude); and (3) if HgCl or HgBr are formed on the surface, desorption and subsequent homogeneous gas-phase reduction of these species to elemental mercury may occur. In the following three subsections, we discuss the plausibility of each of these potential roles using results from our DFT calculations. Similar to Section 3.3, results for each surface will be presented separately in small paragraphs in the order of: (1) OH-Fe-R; (2) $(\text{OH})_3\text{-Fe-R}$ and $(\text{OH})_3\text{-R}$; (3) O-Fe-R; and (4) $\text{Fe-O}_3\text{-R}$ and $\text{O}_3\text{-R}$.

3.4.1. Photocatalytic Hg-X bond-breaking on iron-oxide surfaces

As discussed in the previous sections, our calculations suggest that the activation energy barrier for bond breaking in adsorbed HgX_2 and HgX are, in general, too large to be overcome by thermal effects alone in the temperature range relevant to tropospheric processes. Therefore, photons may play a key role in promoting Hg-X bond dissociation and in mercury reduction on the iron-oxide surface through a process

involving charge transfer from the iron-oxide surface to the oxidized mercury cation.

To address the question whether the photon energy is sufficient to promote this chemistry, we performed band-structure calculations to plot both the total density of states and the partial density of states of mercury for adsorbed HgCl_2 and HgCl on each of the studied surfaces (see Figure S5). Using these band structures, we determined the bands corresponding to the valence-band maximum of the iron-oxide surface (VMB_{IO}) in the total density of states plot and the lowest-unoccupied orbital of the adsorbed $\text{HgCl}_2/\text{HgCl}$ (LUMO_{Hg}) in the mercury partial density of states plot. We then calculated the energy difference for exciting an electron from the VMB_{IO} to the LUMO_{Hg} , thereby estimating the excitation energy for adsorbed Hg species on the specific iron-oxide surfaces. Similar to the gas-phase chemistry discussed earlier, we postulate here that electronic excitation to adsorbed HgCl_2 and HgCl can result in a bond-breaking event. Also, our DFT results for gas-phase HgCl_2 and HgBr_2 suggest that the average thermochemical bond-dissociation energies required to break both Hg-X bonds are 2.38 and 2.08 eV, respectively. In the gas phase, the Hg-Cl bonds are therefore stronger than the respective Hg-Br bonds [18,69]. In addition, the excitation energies are lower for gas-phase $\text{HgBr}/\text{HgBr}_2$ as compared to gas-phase $\text{HgCl}/\text{HgCl}_2$ (Table 1). We expect trends for excitation energies for adsorbed HgCl_2 and HgCl to also apply to adsorbed HgBr_2 and HgBr . Therefore, we perform this band-structure study only for adsorbed Hg, HgCl , and HgCl_2 .

The results of our excitation energy calculations are shown in Table 3. On the OH-Fe-R-terminated surface, the activation energy barrier for the first Hg-Cl bond dissociation in adsorbed HgCl_2 was calculated to be 0.51 eV, which could be within the range of thermal energy available to the system at tropospheric conditions. However, if photons are required (e.g., at lower tropospheric temperatures), our calculations suggest that HgCl_2 adsorbed on the surface has mercury states that overlap with the Fermi energy, resulting in either no or a negligible energy gap for electronic excitation from the VMB_{IO} to the LUMO_{Hg} (Figure S5; corresponding adsorption structures can be found in Table S2). Therefore, we predict that the first Hg-Cl bond-breaking step in adsorbed HgCl_2 can be easily promoted by photons if the available thermal energy alone is not sufficient. The second bond-breaking step involves an excitation energy of 2.69 eV. As this excitation energy is below 3.9 eV, the photons available in the troposphere are sufficient to promote the Hg-Cl bond-breaking steps on the OH-Fe-R surface termination.

The first bond-breaking step on the $(\text{OH})_3\text{-Fe-R}$ surface has a small

Table 3

Calculated excitation energies (E_{Excite}) and corresponding photon wavelengths (ν_{Excite}) required to excite an electron from the VMB_{IO} to the LUMO_{Hg} for adsorbed HgCl_2 , HgCl , and Hg on each of the studied surfaces. An entry of “–” indicates that this species is not present on the surface in the reduction pathway, whereas an entry of “SB” denotes that the barriers are small enough (< 0.4 eV) such that photons are not required. An entry of “No gap” signifies that the system is metallic and mercury bands overlap with the Fermi energy. “*” signifies that the step may not need photons under certain ambient temperatures. Photons in the troposphere have energies up to 3.9 eV.

Surface	HgCl_2		HgCl		Hg	
	E_{Excite} (eV)	ν_{Excite} (nm)	E_{Excite} (eV)	ν_{Excite} (nm)	E_{Excite} (eV)	ν_{Excite} (nm)
$\text{Fe-O}_3\text{-R}$	2.21	561	SB	SB	SB	SB
O-Fe-R	SB	SB	SB	SB	2.64	470
$\text{O}_3\text{-R}$	–	–	No gap*	No gap*	No gap	No gap
OH-Fe-R	No gap*	No gap*	2.69	461	2.59	479
$(\text{OH})_3\text{-Fe-R}$	SB	SB	No gap	No gap	SB	SB
$(\text{OH})_3\text{-R}$	No gap	No gap	2.88	431	SB	SB

barrier and does not require photons. Like the first bond-breaking step on the OH-Fe-R surface termination, adsorbed HgCl on the (OH)₃-Fe-R-terminated surface and adsorbed HgCl₂ on the (OH)₃-R-terminated surface have mercury states that overlap with Fermi energy (Figure S5), resulting in negligible energy gaps for electronic excitation. The second Hg-Cl bond-breaking step on the (OH)₃-R surface requires a photon energy of 2.88 eV.

Both bond-breaking steps on the O-Fe-R-terminated surface have activation energy barriers that can be overcome thermally without the need for photons (< 0.5 eV). On the Fe-O₃-R surface termination, an excitation energy of 2.21 eV is needed for photons to assist in the first bond-breaking step in HgCl₂. Yet, the second bond-breaking step on this surface termination does not require photons, as the activation barrier of 0.21 eV can be overcome with thermal effects. The case is similar for adsorbed HgCl on the O₃-R surface termination, but with an activation energy barrier of 0.58 eV, photons may only be necessary to promote bond activation at lower tropospheric temperatures. Nonetheless, our results show that the electronic excitation energy required to promote the second bond-breaking step on the O₃-R surfaces is negligible.

We find that for the bond-dissociation steps with large barriers, the calculated electronic excitation energies are all below the threshold value of 3.9 eV, which means that photons in the troposphere are indeed available for the surface-to-mercury charge transfer, potentially enabling non-thermal bond-breaking events on the studied iron-oxide surfaces. We propose that this is one potential role of photons in the combined photolytic and heterogeneous reduction pathway for HgCl₂ and HgBr₂ to Hg⁰.

3.4.2. Photon-assisted desorption of atomic mercury

On three of the six surfaces in this study (OH-Fe-R, O-Fe-R, and O₃-R), the adsorption of atomic mercury is strong ($|E_B| > 2$ eV). In particular, on the OH-Fe-R-terminated α -Fe₂O₃(0001) surface, preferentially exposed under normal atmospheric conditions, the adsorption energy of atomic mercury is −2.18 eV. As a result, mercury cannot desorb from this surface under ambient conditions and photons have to promote this process. Our Bader charge analysis (Fig. 4, Section 3.3.3) indicates that the excitation of an electron from the VBM_{IO} to the LUMO_{Hg} to form a neutral mercury adsorbate can significantly weaken the binding energy and allow for mercury desorption as Hg⁰. Accordingly, photons can play a key role in the desorption of mercury from the OH-Fe-R, O-Fe-R, and O₃-R surfaces as long as the excitation energies are below the tropospheric cutoff value of 3.9 eV.

To estimate the excitation energies, i.e., the energies associated with exciting an electron from the surface to the adsorbed mercury cation, we plotted the band structures for the Hg atoms adsorbed on those surfaces which bind Hg strongly (Figure S5). We used these band structures to determine the VBM_{IO} and LUMO_{Hg} and then calculate the energy required to move an electron from the VBM_{IO} to the LUMO_{Hg}. The results of these calculations are summarized in the last two columns of Table 3. On the OH-Fe-R-terminated surface, the excitation energy required to excite an electron from the VBM_{IO} to the LUMO_{Hg} in the adsorbed mercury cation was calculated to be 2.59 eV. On the O-Fe-R surface termination, this excitation energy was determined to be 2.64 eV. On the O₃-R surface termination, we predict a negligible gap for electronic excitation from the VBM_{IO} to the LUMO_{Hg}, as the mercury bands overlap with the Fermi energy. Our calculations suggest that the excitation energies for adsorbed mercury are well within the range of photon energies in the troposphere (< 3.9 eV). We conclude that photons can play a role in assisting in mercury desorption following Hg-X bond-breaking on the iron-oxide surface.

3.4.3. Desorption and gas-phase reduction of HgX

Consistent with the literature, our calculations discussed in Section 3.1 suggest that gas-phase Hg(I) species are easily reducible by photons available in the troposphere [5,7]. Accordingly, one potential role for photons in the reduction of HgCl₂ and HgBr₂ is to break one Hg-X bond

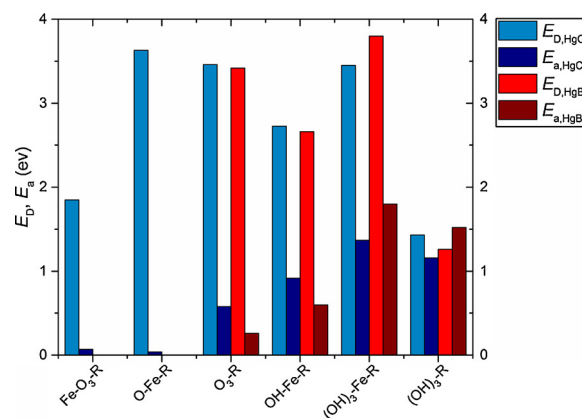


Fig. 5. Desorption (E_D) and activation energy barrier (E_A) for HgCl and HgBr on each of the six iron-oxide surface terminations. Note: an absent bar indicates that the HgCl or HgBr surface intermediate is not stable, as indicated by our reduction energy curves in Figs. 3 and S4 (i.e., both Hg-X bonds are broken in a single, concerted step on the surface). (For interpretation of the references to color in this figure legend, the reader is referred to the web version of this article).

in the adsorbed HgX₂ species; then the resulting HgX surface intermediate desorbs from the surface and undergoes photolytic reduction to Hg⁰ in the gas phase.

To determine the feasibility of this hypothesis, we compared the desorption energy of HgCl (HgBr) with the activation energy barrier required for Hg-X bond-breaking in both adsorbed species on each of the studied iron-oxide surface terminations (see Fig. 5). For each surface, aside from HgBr on (OH)₃-R, the desorption energies are significantly higher than the energies required for bond-breaking. For example, the desorption energy of HgCl (HgBr) on the OH-Fe-R-terminated surface was determined to be 2.73 (2.66) eV; i.e., 1.80 (2.05) eV larger than the energy required for Hg-Cl (Hg-Br) bond-breaking. In addition, the desorption energies are well above 1 eV on every surface, rendering desorption of adsorbed HgX species impossible at tropospheric temperatures only by thermal effects. We also considered the electron-transfer-assisted desorption of HgCl from the studied iron-oxide surfaces, since HgCl tends to adsorb in a cationic form (Table S5). However, because our gas-phase measurements indicate that electronic excitation does promote Hg-Cl bond dissociation (Table 1), we expect that it is more likely for electronic excitations to promote bond dissociation than desorption.

4. Conclusions

We performed DFT (PW91 + *U*) calculations to determine the combined role of photons and relevant atmospheric α -Fe₂O₃(0001) aerosol surfaces in the reduction of HgCl₂ and HgBr₂ to Hg⁰. Our phase diagram analyses suggest that the OH-Fe-R-terminated surface is the most stable under typical tropospheric conditions. The reaction energy profiles and Δ SCF analyses for the reduction of HgCl₂ and HgBr₂ on this surface suggest that the first Hg-X bond-breaking step on the OH-Fe-R-terminated surface is facile and can take place through either thermal or photochemical effects. However, the second Hg-X bond-breaking step, as well as the desorption of mercury from the surface, are likely to not be overcome with thermal energy alone. Our Δ SCF calculations suggest that Hg-Cl bond breaking in adsorbed HgCl through an electronic excitation from the VBM_{IO} to the LUMO_{Hg} has an excitation energy of 2.69 eV, whereas mercury desorption via a photon-assisted surface-to-adsorbate charge-transfer mechanism requires a photon energy of 2.59 eV. Each of these values is below the cutoff energy of 3.9 eV for the photons available for this process in the troposphere, which is in stark contrast with the excitation energy of 4.98 eV for reducing HgCl₂ in the gas phase. This study provides the first evidence for the

mechanistic understanding of the combined role of photons and atmospheric aerosols in the redox chemistry of atmospheric mercury. The procedure developed here can be readily adapted to a wider range of atmospheric aerosols for this chemistry and to other atmospheric reactions involving aerosol surfaces.

Declaration of Interest

None.

Author Contributions

All authors have given approval to the final version of the manuscript.

Acknowledgements

This work was supported by DOE-BES, Office of Chemical Sciences (grant DE-FG02-05ER15731). Additional funding was provided by the Grainger Wisconsin Distinguished Graduate Fellowship and by the University of Wisconsin–Madison, Office of the Vice Chancellor for Research and Graduate Education with funds from the Wisconsin Alumni Research Foundation. The authors thank Benjamin Chen and Ahmed Elnabawy for their insightful comments on the manuscript. Computational work was performed in part on external computing resources at the following institutions: The National Energy Research Scientific Computing Center (NERSC); the Center for Nanoscale Materials (CNM) at Argonne National Laboratory (ANL); and the Environmental Molecular Sciences Laboratory (EMSL), a national scientific user resource located at Pacific Northwest National Laboratory (PNNL). NERSC and CNM are supported by the U.S. DOE, Office of Science, under Contract Nos. DE-AC02-05CH11231 and DE-AC02-06CH11357, respectively. EMSL is supported by the DOE Office of Biological and Environmental Research at PNNL.

Appendix A. Supplementary data

Supplementary material related to this article can be found, in the online version, at doi:<https://doi.org/10.1016/j.apcatb.2018.04.049>.

References

- [1] A.P. Rutter, J.J. Schauer, The impact of aerosol composition on the particle to gas partitioning of reactive mercury, *Environ. Sci. Technol.* 41 (2007) 3934–3939.
- [2] A.P. Rutter, J.J. Schauer, The effect of temperature on the gas-particle partitioning of reactive mercury in atmospheric aerosols, *Atmos. Environ.* 41 (2007) 8647–8657.
- [3] M. Vahedpour, M. Tozihi, F. Nazari, Mechanistic study on the ozone-mercury reaction and the effect of water and water dimer molecules, *J. Chin. Chem. Soc.* 58 (2011) 398–407.
- [4] B. de Foy, Y. Tong, X. Yin, W. Zhang, S. Kang, Q. Zhang, G. Zhang, X. Wang, J.J. Schauer, First field-based atmospheric observation of the reduction of reactive mercury driven by sunlight, *Atmos. Environ.* 134 (2016) 27–39.
- [5] Y. Tong, T. Eichhorst, M.R. Olson, J.E. McGinnis, I. Turner, A.P. Rutter, M.M. Shafer, X. Wang, J.J. Schauer, Atmospheric photolytic reduction of Hg(II) in dry aerosols, *Environ. Sci. Processes Impacts* 15 (2013) 1883–1888.
- [6] Y. Tong, T. Eichhorst, M.R. Olson, A.P. Rutter, M.M. Shafer, X. Wang, J.J. Schauer, Comparison of heterogeneous photolytic reduction of Hg(II) in the coal fly ashes and synthetic aerosols, *Atmos. Res.* 138 (2014) 324–329.
- [7] W.H. Schroeder, J. Munthe, Atmospheric mercury - An overview, *Atmos. Environ.* 32 (1998) 809–822.
- [8] D. Obrist, Y. Agnan, M. Jiskra, C.L. Olson, D.P. Colegrove, J. Hueber, C.W. Moore, J.E. Sonke, D. Helmig, Tundra uptake of atmospheric elemental mercury drives arctic mercury pollution, *Nature* 547 (2017) 201–204.
- [9] M.S. Landis, J.V. Ryan, A.F.H. ter Schure, D. Laudal, Behavior of mercury emissions from a commercial coal-fired power plant: the relationship between stack speciation and near-field plume measurements, *Environ. Sci. Technol.* 48 (2014) 13540–13548.
- [10] P. Holmes, K.A.F. James, L.S. Levy, Is low-level environmental mercury exposure of concern to human health? *Sci. Total Environ.* 408 (2009) 171–182.
- [11] M. Gustin, D. Jaffe, Reducing the uncertainty in measurement and understanding of mercury in the atmosphere, *Environ. Sci. Technol.* 44 (2010) 2222–2227.
- [12] M.A. Alghamdi, M. Almazroui, M. Shamy, M.A. Redal, A.K. Alkhalaf, M.A. Hussein, M.I. Khoder, Characterization and elemental composition of atmospheric aerosol loads during springtime dust storm in western Saudi Arabia, *Aerosol Air Qual. Res.* 15 (2015) 440–453.
- [13] N. Chinnam, S. Dey, S.N. Tripathi, M. Sharma, Dust events in Kanpur, northern India: Chemical evidence for source and implications to radiative forcing, *Geophys. Res. Lett.* 33 (2006) L08803–L08806.
- [14] S.K. Mishra, S. Dey, S.N. Tripathi, Implications of particle composition and shape to dust radiative effect: A case study from the Great Indian desert, *Geophys. Res. Lett.* 35 (2008) L23814–L23818.
- [15] I. Mori, M. Nishikawa, T. Tanimura, H. Quan, Change in size distribution and chemical composition of kosa (Asian dust) aerosol during long-range transport, *Atmos. Environ.* 37 (2003) 4253–4263.
- [16] B.D. Garg, S.H. Cadle, P.A. Mulawa, P.J. Groblicki, C. Laroo, G.A. Parr, Brake wear particulate matter emissions, *Environ. Sci. Technol.* 34 (2000) 4463–4469.
- [17] T. Grigoratos, G. Martini, Brake wear particle emissions: A review, *Environ. Sci. Pollut. Res.* 22 (2015) 2491–2504.
- [18] S.A. Tacey, L. Xu, M. Mavrikakis, J.J. Schauer, Heterogeneous reduction pathways for Hg(II) species on dry aerosols: A first-principles computational study, *J. Phys. Chem. A* 120 (2016) 2106–2113.
- [19] J. Wilcox, A kinetic investigation of high-temperature mercury oxidation by chlorine, *J. Phys. Chem. A* 113 (2009) 6633–6639.
- [20] R.N. Slinger, J.C. Kramlich, N.M. Marinov, Towards the development of a chemical kinetic model for the homogeneous oxidation of mercury by chlorine species, *Fuel Process. Technol.* 65–66 (2000) 423–438.
- [21] S. Niksa, N. Fujiwara, Predicting extents of mercury oxidation in coal-derived flue gases, *J. Air Waste Manage. Assoc.* 55 (2005) 930–939.
- [22] A. Fry, B. Cauch, G.D. Silcox, J.S. Lighty, C.L. Senior, Experimental evaluation of the effects of quench rate and quartz surface area on homogeneous mercury oxidation, *Proc. Combust. Inst.* 31 (2007) 2855–2861.
- [23] J.-E. Jung, D. Geatches, K. Lee, S. Aboud, G.E. Brown Jr., J. Wilcox, First-principles investigation of mercury adsorption on the α -Fe₂O₃(1102) surface, *J. Phys. Chem. C* 119 (2015) 26512–26518.
- [24] A.D. Jew, E.C. Rupp, D.L. Geatches, J.-E. Jung, G. Farfan, L. Bahet, J.C. Hower, G.E. Brown Jr., J. Wilcox, Mercury interaction with the fine fraction of coal-combustion fly ash in a simulated coal power plant flue gas stream, *Energy Fuels* 29 (2015) 6025–6038.
- [25] J. Wilcox, T. Okano, Ab initio-based mercury oxidation kinetics via bromine at postcombustion flue gas conditions, *Energy Fuels* 25 (2011) 1348–1356.
- [26] B.W. Vosteen, R. Kanefke, H. Köser, Bromine-enhanced mercury abatement from combustion flue gases – Recent industrial applications and laboratory research, *VGB Powertech.* 86 (2006) 70–75.
- [27] S.-H. Liu, N.-Q. Yan, Z.-R. Liu, Z. Qu, H.P. Wang, S.-G. Chang, C. Miller, Using bromine gas to enhance mercury removal from flue gas of coal-fired power plants, *Environ. Sci. Technol.* 41 (2007) 1405–1412.
- [28] G. Kresse, J. Furthmüller, Efficiency of ab-initio total energy calculations for metals and semiconductors using a plane-wave basis set, *Comput. Mater. Sci.* 6 (1996) 15–50.
- [29] G. Kresse, J. Furthmüller, Efficient iterative schemes for ab initio total-energy calculations using a plane-wave basis set, *Phys. Rev. B* 54 (1996) 11169–11186.
- [30] J.P. Perdew, Y. Wang, Accurate and simple analytic representation of the electron-gas correlation energy, *Phys. Rev. B* 45 (1992) 13244–13249.
- [31] P.E. Blöchl, Projector augmented-wave method, *Phys. Rev. B* 50 (1994) 17953–17979.
- [32] G. Kresse, D. Joubert, From ultrasoft pseudopotentials to the projector augmented-wave method, *Phys. Rev. B* 59 (1999) 1758–1775.
- [33] S.L. Dudarev, G.A. Botton, S.Y. Savrasov, C.J. Humphreys, A.P. Sutton, Electron-energy-loss spectra and the structural stability of nickel oxide: an LSDA + U study, *Phys. Rev. B* 57 (1998) 1505–1509.
- [34] C. Xu, Y. Zhang, F. Pan, W. Huang, B. Deng, J. Liu, Z. Wang, M. Ni, K. Cen, Guiding effective nanostructure design for photo-thermochemical CO₂ conversion: From DFT calculations to experimental verifications, *Nano Energy* 41 (2017) 308–319.
- [35] C. Xu, Y. Zhang, J. Chen, J. Lin, X. Zhang, Z. Wang, J. Zhou, Enhanced mechanism of the photo-thermochemical cycle based on effective Fe-doping TiO₂ films and DFT calculations, *Appl. Catal. B Environ.* 204 (2017) 324–334.
- [36] G. Rollmann, A. Rohrbach, P. Entel, J. Hafner, First-principles calculation of the structure and magnetic phases of hematite, *Phys. Rev. B* 69 (2004) 165107–165118.
- [37] W. Kudernatsch, G. Peng, H. Zeuthen, Y. Bai, L.R. Merte, L. Lammich, F. Besenbacher, M. Mavrikakis, S. Wendt, Direct visualization of catalytically active sites at the FeO-Pt(111) interface, *ACS Nano* 9 (2015) 7804–7814.
- [38] S.A. Tacey, L. Xu, T. Szilvási, J.J. Schauer, M. Mavrikakis, Quantum chemical calculations to determine partitioning coefficients for HgCl₂ on iron-oxide aerosols, *Sci. Total Environ.* (2018) in press.
- [39] A. Barbier, A. Stierle, N. Kasper, M.-J. Guittet, J. Jupille, Surface termination of hematite at environmental oxygen pressures: Experimental surface phase diagram, *Phys. Rev. B* 75 (2007) 233406–233409.
- [40] L.W. Finger, R.M. Hazen, Crystal structure and isothermal compression of Fe₂O₃, Cr₂O₃, and V₂O₅ to 50 kbars, *J. Appl. Phys.* 51 (1980) 5362–5367, <http://dx.doi.org/10.1063/1.327451>.
- [41] H.J. Monkhorst, J.D. Pack, Special points for brillouin-zone integrations, *Phys. Rev. B* 13 (1976) 5188–5192.
- [42] L. Bengtsson, Dipole correction for surface supercell calculations, *Phys. Rev. B* 59 (1999) 12301–12304.
- [43] J. Neugebauer, M. Scheffler, Adsorbate-substrate and adsorbate-adsorbate interactions of Na and K adlayers on Al(111), *Phys. Rev. B* 46 (1992) 16067–16080.
- [44] G. Henkelman, H. Jónsson, Improved tangent estimate in the nudged elastic band method for finding minimum energy paths and saddle points, *J. Chem. Phys.* 113

- (2000) 9978–9985.
- [45] G. Henkelman, B.P. Uberuaga, H. Jónsson, Climbing image nudged elastic band method for finding saddle points and minimum energy paths, *J. Chem. Phys.* 113 (2000) 9901–9904.
- [46] J. Greeley, M. Mavrikakis, A first-principles study of surface and subsurface H on and in Ni(111): Diffusional properties and coverage-dependent behavior, *Surf. Sci.* 540 (2003) 215–229.
- [47] W. Tang, E. Sanville, G. Henkelman, A grid-based bader analysis algorithm without lattice bias, *J. Phys. Condens. Matter.* 21 (2009) 84204.
- [48] E. Sanville, S.D. Kenny, R. Smith, G. Henkelman, Valence bond theory for chemical dynamics, *J. Comput. Chem.* 28 (2007) 899–908.
- [49] G. Henkelman, A. Arnaldsson, H. Jónsson, A fast and robust algorithm for bader decomposition of charge density, *Comput. Mater. Sci.* 36 (2006) 354–360.
- [50] M. Yu, D.R. Trinkle, Accurate and efficient algorithm for bader charge integration, *J. Chem. Phys.* 134 (2011) 064111–064118.
- [51] T. Kowalczyk, S.R. Yost, T. Van Voorhis, Assessment of the Δ SCF density functional theory approach for electronic excitations in organic dyes, *J. Chem. Phys.* 134 (2011) 054128–054135.
- [52] R.J. Maurer, K. Reuter, Assessing computationally efficient isomerization dynamics: Δ SCF density-functional theory study of azobenzene molecular switching, *J. Chem. Phys.* 135 (2011) 224303–224312.
- [53] M.J. Frisch, G.W. Trucks, H.B. Schlegel, G.E. Scuseria, M.A. Robb, J.R. Cheeseman, G. Scalmani, V. Barone, B. Mennucci, G.A. Petersson, H. Nakatsuji, M. Caricato, X. Li, H.P. Hratchian, A.F. Izmaylov, J. Bloino, G. Zheng, J.L. Sonnenberg, M. Hada, M. Ehara, K. Toyota, R. Fukuda, J. Hasegawa, M. Ishida, T. Nakajima, Y. Honda, O. Kitao, H. Nakai, T. Vreven, J. Montgomery, J.A.J.E. Peralta, F. Ogliaro, M. Bearpark, J.J. Heyd, E. Brothers, K.N. Kudin, V.N. Staroverov, R. Kobayashi, J. Normand, K. Raghavachari, A. Rendell, J.C. Burant, S.S. Iyengar, J. Tomasi, M. Cossi, N. Rega, J.M. Millam, M. Klene, J.E. Knox, J.B. Cross, V. Bakken, C. Adamo, J. Jaramillo, R. Gomperts, R.E. Stratmann, O. Yazyev, A.J. Austin, R. Cammi, C. Pomelli, J.W. Ochterski, R.L. Martin, K. Morokuma, V.G. Zakrzewski, G.A. Voth, P. Salvador, J.J. Dannenberg, S. Dapprich, A.D. Daniels, O. Farkas, J.B. Foresman, J.V. Ortiz, J. Cioslowski, D.J. Fox, Gaussian 09, Revision D.01, (2009).
- [54] J.P. Perdew, K. Burke, M. Ernzerhof, Generalized gradient approximation made simple, *Phys. Rev. Lett.* 77 (1996) 3865–3868.
- [55] C. Adamo, V. Barone, Toward reliable density functional methods without adjustable parameters: The PBE0 model, *J. Chem. Phys.* 110 (1999) 6158–6170.
- [56] R.A. Kendall, T.H. Dunning Jr., R.J. Harrison, Electron affinities of the first-row atoms revisited. Systematic basis sets and wave functions, *J. Chem. Phys.* 96 (1992) 6796–6806.
- [57] D.E. Woon, T.H. Dunning, Gaussian basis sets for use in correlated molecular calculations. III. The atoms aluminum through argon, *J. Chem. Phys.* 98 (1993) 1358–1371.
- [58] A. Schäfer, H. Horn, R. Ahlrichs, Fully optimized contracted gaussian basis sets for atoms Li to Kr, *J. Chem. Phys.* 100 (1994) 5829–5835.
- [59] A. Schäfer, C. Huber, R. Ahlrichs, Fully optimized contracted gaussian basis sets of triple zeta valence quality for atoms Li to Kr, *J. Chem. Phys.* 100 (1994) 5829–5835.
- [60] F. Weigend, R. Ahlrichs, Balanced basis sets of split valence, triple zeta valence and quadruple zeta valence quality for H to Rn: Design and assessment of accuracy, *Phys. Chem. Chem. Phys.* 7 (2005) 3297–3305.
- [61] F. Weigend, Accurate coulomb-fitting basis sets for H to Rn, *Phys. Chem. Chem. Phys.* 8 (2006) 1057–1065.
- [62] NIST-JANAF Thermochemical Tables, National Institute of Standards and Technology, (2013).
- [63] P.J. Hay, W.R. Wadt, L.R. Kahn, F.W. Bobrowicz, *Ab initio* studies of AuH, AuCl, HgH, and HgCl₂ using relativistic effective core potentials, *J. Chem. Phys.* 69 (1978) 984–997.
- [64] R. Chang, Chemistry, 10th ed., New York, NY, 2009.
- [65] EPA, Mercury Study Report to Congress, EPA-452/R-97-003, Office of Air Quality Planning and Standards, Office of Research and Development, US Government Printing Office, Washington, DC, 1997.
- [66] F.S. Rowland, Stratospheric ozone depletion, *Philos. Trans. R. Soc. B.* 361 (2006) 769–790.
- [67] J.K. Nørskov, F. Abild-Pedersen, F. Studt, T. Bligaard, Density functional theory in surface chemistry and catalysis, *Proc. Natl. Acad. Sci.* 108 (2011) 937–943.
- [68] H.S. Fogler, *Essentials of Chemical Reaction Engineering*, 1st ed., Upper Saddle River, NJ, 2010.
- [69] S. Lyman, C. Jones, T. O'Neil, T. Allen, M. Miller, M.S. Gustin, A.M. Pierce, W. Luke, X. Ren, P. Kelley, Automated calibration of atmospheric oxidized mercury measurements, *Environ. Sci. Technol.* 50 (2016) 12921–12927.